

<https://doi.org/10.1038/s41528-024-00314-2>

Evaporation-induced self-assembled ultrathin AgNW networks for highly conformable wearable electronics

Check for updates

Chu Qin¹, Qingyin Sun¹, Yu Chen¹, Shah Fahad¹, Jiaxin Wu¹, Yuxuan Dong¹, Hongyu Yu^{1,2} & Min Wang^{1,2}

The flexibility and stability of transparent electrodes play a crucial role in the growing popularity of flexible devices, especially in potential wearable electronics. To date, various solution-coating techniques have been developed for fabricating silver nanowire (AgNW) flexible bioelectronics. However, achieving the orderly distributed patterns of AgNW without undesirable aggregations still poses a grand challenge. Here, an approach to realize regular patterned ultrathin AgNW networks on a freestanding electrospun PVDF-TrFE frame by evaporation-induced self-assembly is proposed. The patterning mechanism of evaporating AgNW colloidal suspension is investigated from experimental and theoretical analysis. The influence of evaporation-induced flow inside colloidal freestanding membranes on forming regular square hole-shaped arrays, selective deposition of AgNW, and aligning them along the artificial pinning array are addressed. Owing to the orderly arrangement of AgNW networks, the resultant flexible electrode achieves ultrathin thickness (about 5 μm), high optical transmittance (87.8%), and low sheet resistance ($8.4 \Omega\text{-sq}^{-1}$) with a relatively low dosage of AgNW ($9 \mu\text{g}\cdot\text{cm}^{-2}$). The electrode exhibits excellent durability during cyclic bending (50,000 times) and stretching (50% strain). The resistance remains virtually unchanged during 200 days in everyday environments. Furthermore, the excellent conformability and breathability of the flexible transparent electrode attached to the human skin demonstrates its potential application as an e-skin sensor. Our findings reliably urge a simple approach to underscore better outcomes with effective patterns by self-assembly of AgNW for highly conformal wearable electronics.

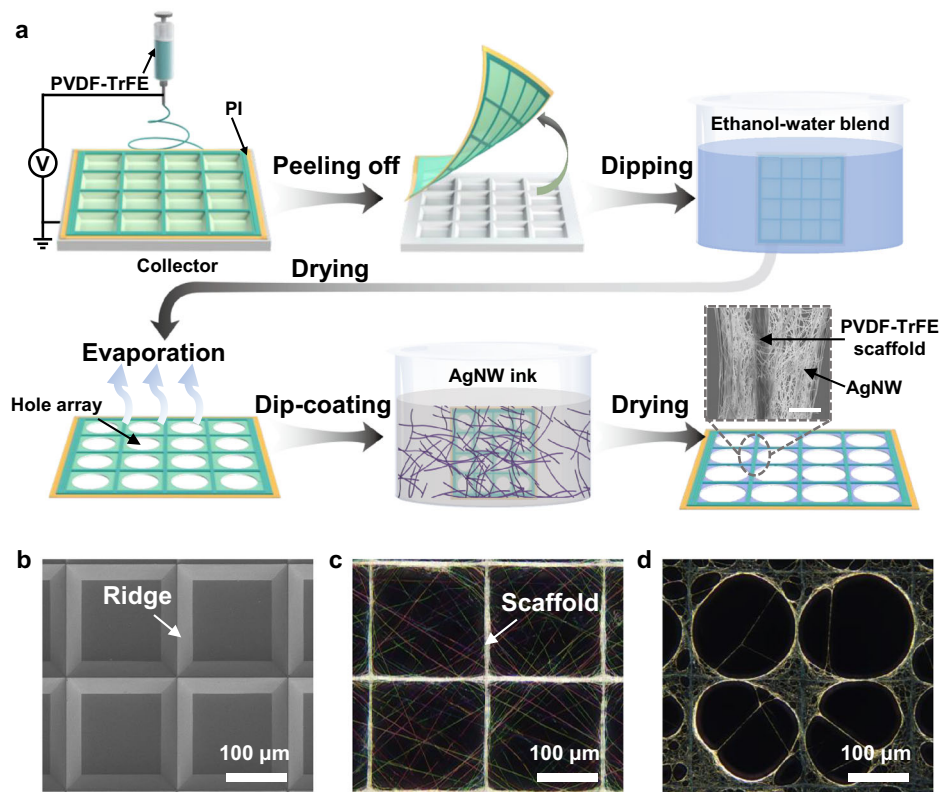
Flexible transparent electrodes (FTEs) play a vital role in numerous next-generation electronic technologies, such as optoelectronic devices^{1–5}, healthcare wearables^{6–10}, and human-machine interfaces^{11–15}. To satisfy the fabrication and application of flexible electronics, FTEs require additional properties like superior conductivity, robustness, durability, and diversity, as well as smaller size and lower cost. Among the various developed materials for conductive pathways in flexible electronics, AgNW has attracted tremendous attention to fabricate FTEs for high electrical conductivity and mechanical flexibility, and the process adaptability of solution processing^{16–19}. To date, enormous solution-based processes, including spin coating²⁰, spray coating²¹, vacuum filtering²², rod or blade coating^{23,24}, printing techniques^{25,26}, and methods based on coffee ring effect^{27–29}, have

been developed for fabricating AgNW FTEs. However, current solution-based techniques still can hardly place the nanowires at the desired position with controllable accumulation density, which usually leads to random distribution and aggregation of nanowires. Significant AgNW dosage is needed to attain improved conductivity, which not only increases the cost but also sacrifices the transmittance³⁰. Besides, the uniformity of the deposited AgNW decreases drastically as the area increases. Han et al. reported a facile 2D ice-templating approach to fabricate large-area AgNW patterns on various substrates³¹. During ice crystal growth, AgNW were effectively aligned and compacted, yielding high contact area, low contact resistance, and excellent mechanical durability. Another solution-based assembly method of AgNW endowed accumulation of AgNW at the edges

¹School of Microelectronics, Southern University of Science and Technology, Shenzhen 518055, PR China. ²Engineering Research Center of Integrated Circuits for Next-Generation Communications, Ministry of Education, Southern University of Science and Technology, Shenzhen 518055, PR China.

e-mail: wangm@sustech.edu.cn

Fig. 1 | Fabrication and structure of AgNW networks. **a** Schematic illustration of the fabrication process for AgNW networks, and the inserted SEM image of AgNW wrapped around PVDF-TrFE scaffold. Scale bar: 5 μm . **b** SEM image of the silicon mold. **c** Optical image of the free-standing PVDF-TrFE film. **d** Optical image of the AgNW patterning.



of the droplets during spraying enabled by a scalable coffee-ring effect³². Zhao et al. presented a flow-driven self-assembly for preparing the highly oriented woven AgNW grids with a silicon templating³³. Although the above methods have led to significant advances in the conductivity and transparency of flexible electronics by assembling AgNW into specific pattern using the solution-based approach, there are still some unresolved issues. For example, the facile 2D ice-templating approach can assemble AgNW efficiently, and yet it has strict limits due to the difficulty of controlling the specific growth of ice crystals. The self-assembly scheme using coffee ring effect needs to control droplet distribution and evaporation behavior on the substrate, otherwise it will lead to the random distribution and undesirable aggregation of AgNW. The silicon template is utilized to arrange AgNW into regular grids but suffers from the damage during subsequent transferring process. Despite these efforts, controllable patterning of AgNW-based FTEs by using a solution process remains a challenge.

Here, we report an evaporation-induced self-assembly approach to obtain a free-standing AgNW networks. A uniform conductive nanowires patterning is obtained on a predesigned PVDF-TrFE frame by solvent evaporation of a AgNW-colloidal suspension. The electrode shows ultrathin thickness (about 5 μm), high optical transmittance (87.8%), and low sheet resistance ($8.4 \Omega\text{-sq}^{-1}$) with a relatively low AgNW dosage ($9 \mu\text{g}\cdot\text{cm}^{-2}$)³¹. It also exhibits excellent durability during cyclic bending (50,000 times with a bending radius of 2 mm) compared to the commercial ITO/PET. After 200 days in an everyday environment, the resistance of the pattern only increased by 1.6 Ω . Additionally, we demonstrated the potential applications of our electrode in wearable electronics for electrophysiological (ECG) and electromyography (EMG) monitoring. With its versatility and controllability, we believe that the evaporation-induced self-assembly is encouraging to large-area nanostructures patterning on a pilot scale.

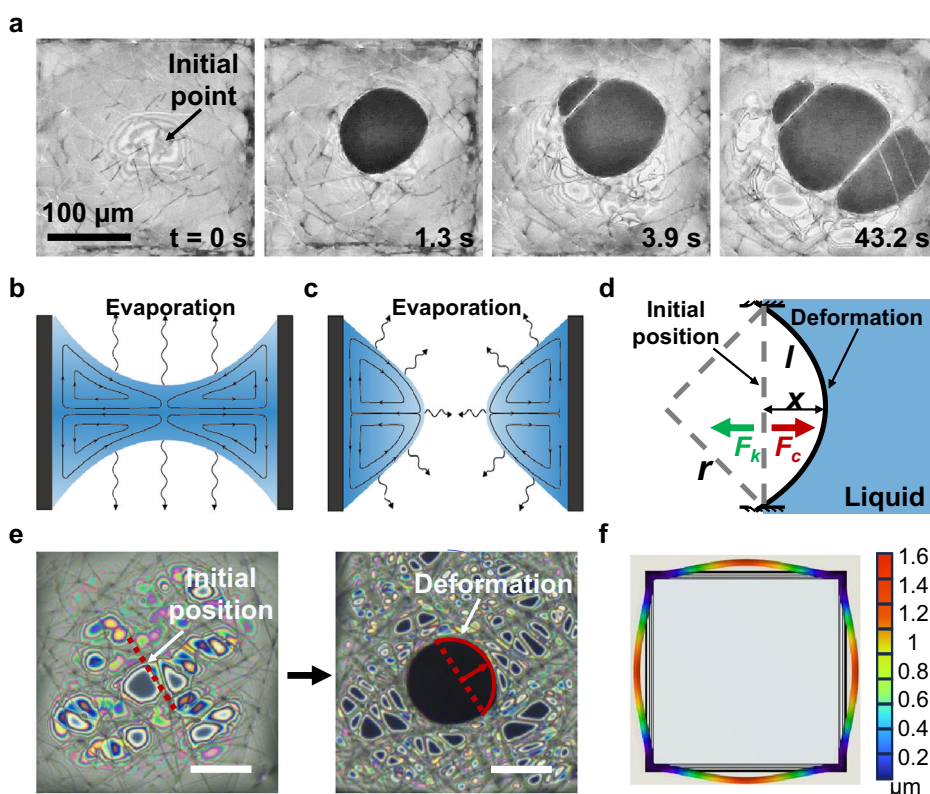
Results

Design of fine patterned AgNW network FTE and its preparation procedure

The fabrication procedure divided into three major steps is outlined in Fig. 1a, and the details can be found in the experimental section. Step 1 is the

prefabrication of the electrospun nanofibrous framework. To obtain a selectively deposited PVDF-TrFE scaffold, a silicon mold with an invested pyramid structure was used, as shown in Fig. 1b. These square-pyramidal cavities, prepared by photolithography technique and anisotropic wet etching of silicon, create height differences in the surface topology depicted in the Supporting Information note 1. Subsequently, a current collector of 300 nm thick silver was deposited onto it. It is noted that the enhanced conductivity of metallic collector contributes to the selective deposition of electrospun nanofibers³⁴. This phenomenon is well-analyzed and stimulated in the Supporting Information note 2. Additionally, a laser-cutting Polyimide (PI) shadow mask was used to define the region of interest, which can not only easily separate the electrospun film from the collector without wrinkles but also ensure the flatness and structural regularity of nanofiber film. Then, nanofibers with diameter range from 400 nm to 1000 nm were prepared by electrospinning a PVDF-TrFE solution onto the collector and regularly intertwined to form a fibrous patterning structure. Generally, the PVDF-TrFE fibers are preferentially deposited on the raised grid under the action of a boosted electric field to form a mesh-like pattern. Such a special electric field focusing effect tends to be weakened gradually with the electrospinning time increasing³⁵. Accordingly, there were some fibers inside the grids, which may blur the array pattern and degradation the performance of the optical transmission. After peeling off from the collector, a suspended electrospun nanofiber film along with the frame was obtained (Fig. 1c). Step 2 is the refinement of the electrospun scaffold by evaporative ethanol-water blend, which favors the formation of more regular patterns for nanowires placement. After withdrawing from the blend, the thickness of suspended liquid membrane decreases due to quick evaporation and eventually leads to the rupture of the liquid membrane and the enlargement of regular holes. Periodic patterns in space and time can be observed in individual grids of PVDF-TrFE frame. Consequently, the nanofibers inside the grids are dragged toward the electrospun scaffolds during symmetrical evaporation of hanging membranes. The dip-dry process can be cycled several times to achieve desired scaffold. The final step is evaporative self-assembly of AgNW-colloidal suspension. With the solvent evaporation, AgNW are pinned and tangled together to form continuous networks around the

Fig. 2 | Schematic illustration and simulation of hole-opening process. **a** Liquid film evaporation rupture under high-speed camera. **b** Side view of thin liquid film. **c** Side view of rupture of thin liquid film. **d** Schematic of fiber displacement. **e** Optical image of nanofibers displacement under surface tension. Scale bar: 25 μm . **f** Simulated deformation displacement of nanofibers during evaporation. Grid size: 50 μm . Deformation ratio: 1.



PVDF-TrFE scaffolds. The conductivity of the pattern strongly depends on the density of AgNW coating. A free-standing FTE with orderly organized AgNW is successfully obtained, as shown in Fig. 1d. It is noted that the AgNW only wrapped around the two-dimensional plane formed by the hole-opened PVDF-TrFE film. Therefore, the film thickness is extremely thin (about 5 μm), which is demonstrated in supplementary Figure 3.

Evaporation-induced refinement of hole-array

As mentioned above, the refinement of electrospun templating is vital for controllable patterning of AgNW. In the following, a description of evaporation of an ethanol hanging membrane is presented and the influence of geometrical parameters on hole-array formation is investigated thereafter. Experiments were conducted in a clean room with steady temperature and humidity. An electrospun PVDF-TrFE free-standing film with $200 \times 200 \mu\text{m}$ square array on carrying PI substrate was utilized as the templating. The drying process was observed in situ under an optical microscope (Supplementary Video 1). Figure 2a shows the hole-array refinement with respect to the evaporation proceeding. The evaporation-induced hole-opening process can be divided into four successive phases: formation of thin liquid film, rupture of liquid film, growth of the holes, and the formation of regular hole-array, as shown in Supplementary Figure 4.

First, a suspended liquid film was formed after withdrawn from the solution. A force balance can be obtained among gravitational, pinning and surface tension forces all at once. During the continuous evaporation of the solvent of ethanol, the competition between thermogravimetry and thermocapillary can be evaluated by the dimensionless Bond number, which can be expressed by $B_0 = \rho gh^2/\sigma$ (where ρ is the liquid density, g is the gravitational acceleration, h is the wetting height of the pinned membrane and σ is the surface tension). For our case, Bond number is much less than the order of 1, which means the capillary force dominates gravity, namely the capillary flow in the interior liquid dominates gravity flow. Therefore, the liquid with low volume fractions can be suspended in the air with the support of the bezel and will not drip under the influence of gravity^{36,37}. The evaporation motion was constrained by the solid wall boundary (PVDF-TrFE nanofibers), which should be considered as a special type of liquid bridge³⁸. Due to

the suspended geometrical feature and symmetrical evaporative flux, a symmetrical capillary bridge with critical liquid volume and critical curvature of the liquid film meniscus was generated between fibers. The second stage is liquid film rupture. For individual pinning grids, one can suppose that evaporation was greatest at the center of the free-standing membrane and nearly zero at the edge of grids. Therefore, a temperature difference occurs at the free interface of the liquid film due to rapid evaporation, which caused a surface tension-driven flow, as shown in Fig. 2b. Such interior flow is named as Marangoni eddy. With the drop of the total volume of blend, a periodic pattern in space and time was observed due to the thinning of the liquid film. Normally, the central part shows the minimum liquid film height. Thus, the film fragmentation here refers to the part of the liquid film that is preferentially ruptured in the central area of the pixel due to uneven evaporation. In Fig. 2c, this liquid film rupture is the combined action by a complex interplay between the intermolecular attractive van der Waals forces, capillarity, and hydrodynamics. This interplay results in a critical thickness at which attractive intermolecular forces dominate, thus causing film rupture³⁹. If the thickness of such films is of or less than the order of a micrometer, long-range intermolecular forces become significant and influence the thinning dynamics^{40,41}. The third stage is hole-growth. The rupture point will immediately become a round hole of tens of microns under surface tension⁴². Thus, as evaporation proceeds, the liquid film gradually shrinks, and the holes become larger and larger. In the liquid film portion around the opening hole, the force of surface tension acts tangentially to the surface, as shown by the red arrow in Fig. 2d. The contraction of the liquid film causes these fibers to move closer to the edge of the grid, increasing the porosity of the liquid film. At the same time, the evaporation of the remaining liquid between the fibers favors the fiber aggregation, which in turn contributes to the expanding of pores. Corresponding to surface tension is the viscous force of the liquid film. Due to the properties of the ethanol-water blend, it is much less than the surface tension. As a result, the holes in the liquid film become larger and larger, and the fibers are dragged away from the initial positions. Figure 2e shows the fiber displacement behavior observed under an optical microscope in situ. The fourth stage is completely evaporation and therefore the formation of a

regular pore pattern among individual ridges. As solvent evaporated, the distance decreases until the contact of two wires where the capillary force reaches maximum. It is noted that the coalescence of fibers is irreversible. That is, even after the liquid is fully evaporated, the fibers remain bond together, possibly due to the van der Waals force⁴³. Especially, a single fiber produces obvious displacement under the action of surface tension. Meanwhile, the coalescence is also affected by fibers' rigidity and electrospun structure.

The size of the enlarged pore is mainly determined by the nanofiber properties and the surface tension of the liquid. The experiment shows that a nonuniform temperature perturbation produced along the surface resulted in a surface tension gradient, which pulled the surface fluid toward regions of higher surface tension (i.e., the PVDF-TrFE grid edge regions). With increasing the evaporative time, the blend concentration altered due to a decrease of the temperature difference, which implied a surface tension change. It is observed that the scattered nanofibers were elongated under surface tension. As shown in Fig. 2c, an equilibrium between the liquid surface tension F_c and fiber elastic recovery force F_k was created and eventually formed a bending curvature of R . Note that the cracked liquid film has surface tension on both sides. Thus, the mechanical model of nanofiber deformation follows an elastic rod fixed at both ends, which can be described by the formula⁴⁴:

$$\delta x = 4 \frac{\gamma R}{k} \arcsin\left(\frac{1}{2R}\right) \quad (1)$$

where x is the deformation of the fiber along the surface tension worked on fibers. k is the elastic coefficient of nanofiber. γ is the surface tension coefficient of liquid. l is the effective length of the surface tension applied to the nanofiber. The nanofiber is prepared by electrospinning using PVDF-TrFE material with the Young's modulus 20.8 MPa^{45,46}. The elastic coefficient of nanofiber is calculated by $k = 24EI/l^3$, where I is the area inertia moment ($I = \pi r^4/4$, r is the radius of the nanofiber). The elastic coefficient k is 35 mN·m⁻¹ ($r = 3 \mu\text{m}$, $l = 50 \mu\text{m}$). Considering the effect of the viscous force of liquid on surface tension and evaporation rate, an ethanol-water blend was used to improve the porosity of FTEs, and the ratio determines the size of the hole by Eq. 1. The surface tension coefficient of the liquid γ is 20.8 mN·m⁻¹ at 20°C⁴⁷. Therefore, the deformation of nanofiber caused by bending can be calculated as x is 12 μm and the radius of hole R is 33 μm . Moreover, changing the ratio of ethanol-water blend will change the surface tension, resulting in a different hole radius from 25 to 40 μm .

To prove the above theoretical analysis, using COMSOL Multiphysics to simulate deformation of nanofiber during evaporation is evidenced in Fig. 2f. The results show the deformation of nanofiber under surface tension is 1.5 μm , which is in good agreement with the theoretical analysis results.

AgNW deposition in evaporative colloidal suspension

To deposit AgNW on the suspended substrate deposition, an evaporative colloidal suspension was utilized by a mixture of AgNW ink and ethanol-water blend. For the binary phase suspension, the evaporation is performed in a similar way to the pure blend described above. The difference is the deposition of nanowires. For instance, AgNP can also be self-assembled onto the free-standing film with hole array induced by liquid film rupture¹⁶. The solid phase settlement on the enlarged scaffold will be described emphatically in this part. It is noted that the manner in which the solvent evaporates from the suspension should significantly affect the interior flow of the suspension.

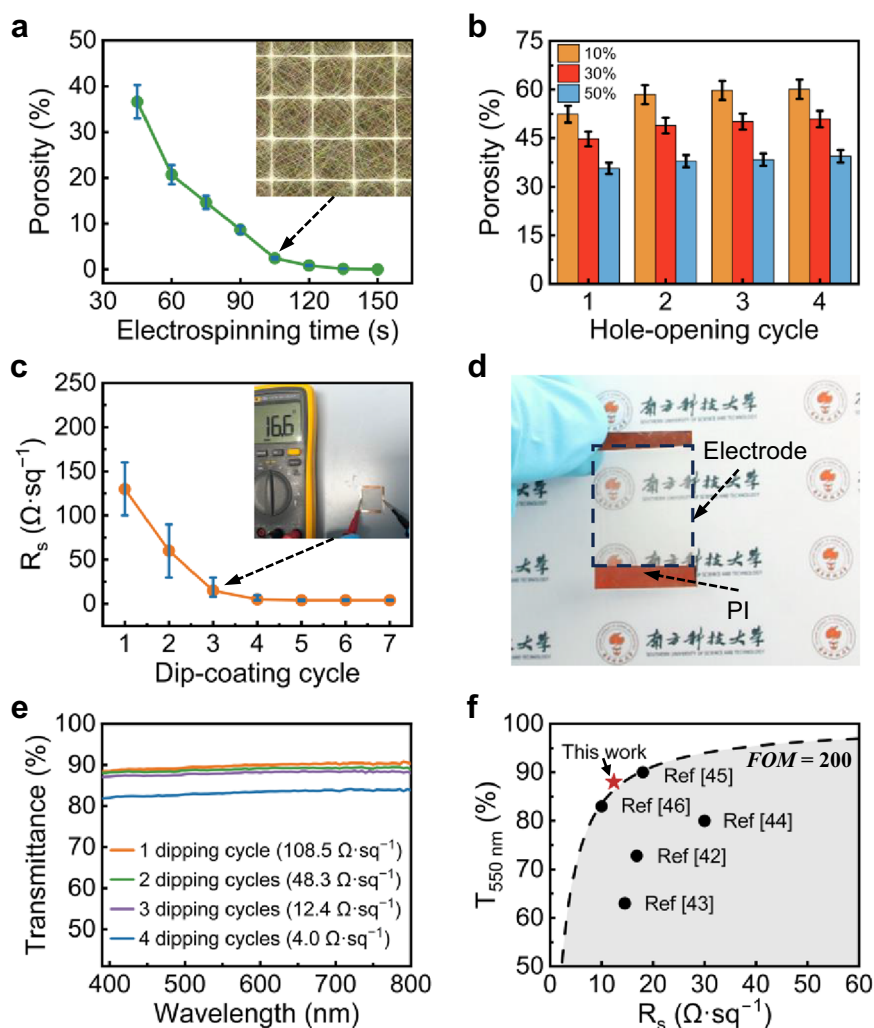
Initially, the colloidal suspension has a uniform distribution of AgNW. In the interior of the suspension, the nanowires concentration is relatively low, and pressure gradients can be balanced by viscous stress, which is well-known in Stokes flow⁴⁸. Therefore, it is assumed that the colloidal nanowires have a negligible effect on the hydrodynamics inside the suspension. Under a nonuniform evaporation, an inward flow of liquid toward the center of the film is required for mass conservation, which converts the nanowires away from the contact line, reducing the nonuniformity of nanowires in the

suspension. As the evaporation proceeds, the AgNW tend to aggregate near the edge of grids and forms the redistribution of the nanowires. Upon complete evaporation of the solvent, the suspended nanowires remain adhered to the PVDF-TrFE fibers to form an ordered structure. The pinning is due to the colloidal nanowires wedging between the PVDF-TrFE and solid-liquid interface physically, the contact line remains pinned because of the accumulation of colloidal nanowires at the surface of PVDF-TrFE fibers. The density of developing AgNW coating along the fiber framework depends on the amount of time that the pins at a particular location. Besides, suspension grid geometry is also found to affect the evaporation-induced flow, with concave regions along the contact lines experiencing a lower evaporative flux. Using in-situ observation, we acquired images of woven nanowires along the edges of grids, consistent with accumulated liquid volume near the edges. The pattern of AgNW can be also tuned by controlling the evaporation in grids.

Performance evaluation of as-fabricated FTE

Apparently, the electrospinning time plays a major role in determining the nanofiber density and porosity within individual grid. Porosity is the ratio of the area of the fiber portion to the area of the blank portion. The porosity of the electrode can be calculated the with Image J, which can reflect the effect of hole-opening on the morphology of the film. As shown in Fig. 3a, the shorter the spinning time, the better the selective deposition of fibers, and the higher the porosity. Since the films electrospun for 45 s were too fragile to test, the 1 min films were selected for follow-on operation. Then, the electrospun films were submerged into different concentrations of ethanol solution for hole-opening. As explained above, the concentration of the ethanol solution affects the surface tension of the solution, which in turn affects the effect of hole opening and porosity. The ethanol-water blend of 10 wt% ethanol addition has the surface tension coefficient of 50.0 mN·m⁻¹, which is higher than 30 wt% and 50 wt% ones⁴⁷. Figure 3b shows that 10 wt % ethanol solution causes the highest porosity for the same hole-opening time. Therefore, the 10 wt% ethanol concentration was used by us in the experiment. And after twice hole-opening, the porosity did not increase significantly, which is due to the aggregation of fibers to make it resist the effect of surface tension. The conductivity of the film is conferred by coating AgNW. It is obvious that the AgNW content of the film increases as the number of coating increases. It is calculated that the AgNW content of free-standing film increases by about 4.5 $\mu\text{g}\cdot\text{cm}^{-2}$ per coating cycle. As presented in Fig. 3c, the sheet resistance of the film decreases as the number of coating increases. For the first three coating cycles, the sheet resistance of the film significantly decreases with the loading of the AgNW. The initial deposition of AgNW onto PVDF-TrFE scaffold may result from the electrostatic attraction between oppositely charged components⁴⁹. With the coating process continues, the attraction force becomes weaker, leading to a slower deposition rate of AgNW. On the other hand, the conductivity and resistance of the as-fabricated electrode can reach a relative saturation value after AgNW density exceed a critical value. Thus, subsequent tests were performed using samples coated three times with AgNW. A piece of square-shaped sample is shown in Fig. 3d to demonstrate its excellent optical transmittance due to its ultra-thin structure. The overall optical transmittance spectra with different sheet resistance are exhibited in Fig. 3e. It is noted that the increase of AgNW dosage decreases the transmission of the electrode while increasing the conductivity. For the sample having a sheet resistance of 12.4 $\Omega\cdot\text{sq}^{-1}$, the transmittance at 550 nm wavelength is found to be 87.8%. To compare the properties of FTEs and previous presented AgNW-based electrodes, the figure of merit⁵⁰ (FOM) has been introduced to characterize the relationship between light transmittance and sheet resistance. The higher the FOM value, the better the properties of the transparent electrode. As shown in Fig. 3f, most electrodes have the FOM value of no more than 200 (the dashed line). The free-standing hole-opened electrodes demonstrates much lower sheet resistance and higher FOM value. The hole-opened structure and excellent conductivity of the electrode contributes to the high FOM value, which is superior to most of the recently reported flexible transparent electrodes.

Fig. 3 | Optical and electrical characterizations of the electrodes. **a** Electrospun film porosity variation with spinning time. **b** Variation of porosity of spun films immersed in different concentrations of ethanol-water blend with the number of hole-opening cycles. **c** Sheet resistance of the electrodes with different dip-coating cycles. **d** Optical image of as-prepared electrode indicating its transmittance. **e** Transmittance of the electrodes with different dip-coating cycles. **f** Comparison of our work with some reported previous excellent AgNW electrodes^{18,52–55}.



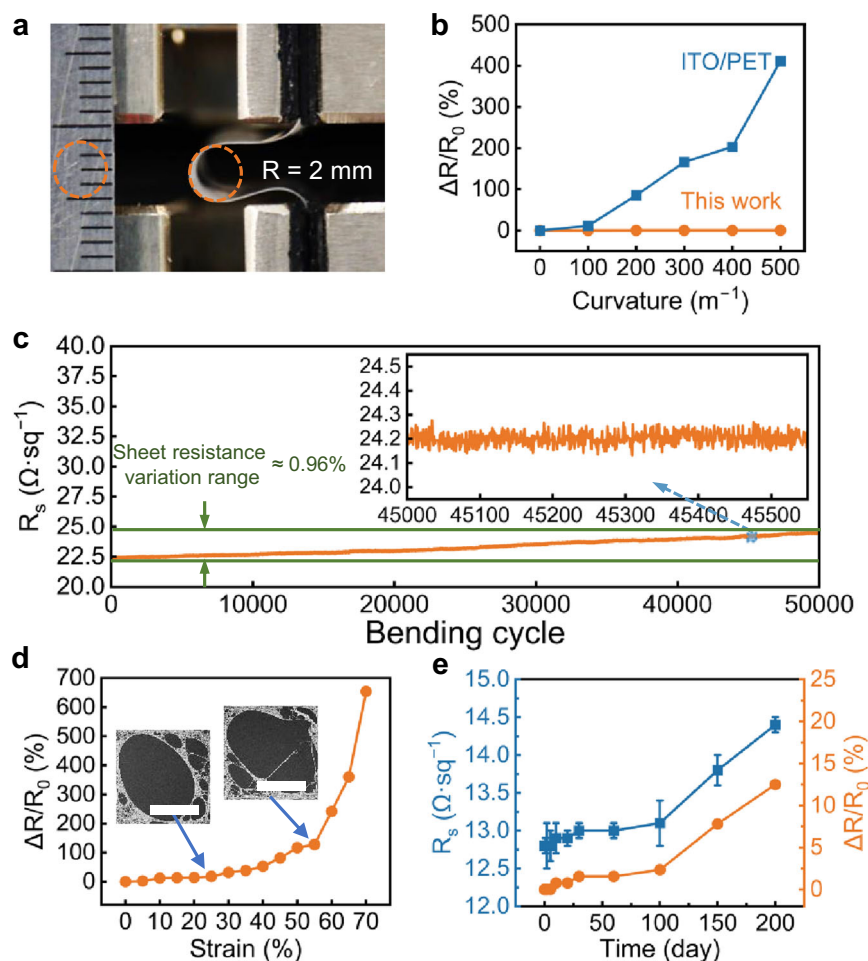
The robustness and durability of electrodes in flexible electronics are the most relevant aspects for its potential applications. In this regard, the mechanical stability of sheet resistance during bending, cyclic bending, and stretching were investigated. For the bending test, the electrode was transferred onto a 25 μm thick PI substrate that was clamped and held in the same bending shape. Figure 4a shows the optical images of the electrode at a maximum bending curvature of 500 m^{-1} (bending radius 2 mm). As the distance between the clamps decreases, the radius of curvature decreases, the curvature of the film increases. Figure 4b compares the sheet resistance variation ($\Delta R/R_0$) of this work and commercial ITO/PET electrode at different bending curvatures of 0 m^{-1} , 100 m^{-1} , 200 m^{-1} , 300 m^{-1} , 400 m^{-1} , and 500 m^{-1} , respectively. The sheet resistance of the electrode even slightly increases as a maximum curvature of bending is applied. At the maximum curvature of 500 m^{-1} , the resistance changes by merely 0.37%, which is sharply contrasted to the ITO/PET electrode (411.583%). As shown in Fig. 4c, the free-standing porous electrodes maintains low sheet resistance variation (0.96%) even after bending 50,000 cycles. The inserted figure depicts the sheet resistance fluctuation of the electrode as the bending proceeds, which implies that the influence of each bending cycle on the sheet resistance of the film is extremely slight. It is likely attributed to the fact that bending deformation does not have a significant effect on very thin structures. The morphology of the electrode after bending 50,000 cycles is shown in Supplementary Fig. 6, the squared array structure is basically free of deformation and damage, which demonstrates the excellent robustness of the ultrathin electrode. Figure 4d illustrates the sheet resistance variation of the electrodes during stretching test. Quantitatively, as the electrode is stretched to 50% strain, the increase of sheet resistance of the electrodes is

116.57%. The insets in Fig. 4d describe the morphology of the deformation of AgNW network when the electrode undergoes stress. Left inset shows the stress is loaded almost solely onto the nanofiber-based backbone and contributes to the deformation of the network. In other words, the conductive path can survive the strain unless the network is broken. As shown in Supplementary Figure 8, the hysteresis curve of the electrode resistance variation during stretching-releasing cycles, which also illustrates the robustness of the electrode. The network structure prepared by electrospinning supported and stabilized the contacts among the AgNW, which is vital for the excellent robustness. Furthermore, the free-standing porous electrode is found to have quite stable conductivity in an ambient atmosphere. After 200 days, the extremely small resistance variation (12.5%, sheet resistance increases 1.6 Ω) is obtained (Fig. 4e). All the results above justify the robustness and stability of the electrodes.

The biology application demo of FTE

To demonstrate the potential bioelectric applications of this sample, an ECG/EMG signal monitoring sensor was fabricated. Figure 5a shows a sample with an area of 2.5 cm \times 2.5 cm worn on the arm. By spraying alcohol onto the skin, the electrode film can be easily attached to the skin even with full of wrinkles and tiny channels. It is obvious that the electrode fits tightly on the skin which is due to its ultra-thin feature. Owing to the excellent optical transmittance, it is almost invisible except for the conductive connection part. In Fig. 5a (i, ii), optical microscopy observes the conformability of electrodes to the skin in its squeezing state and in the stretching state. Moreover, the ultra-thin electrodes have sufficient tensile properties to

Fig. 4 | Mechanical properties of free-standing porous electrodes. **a** Optical images of a sample on the PI film at a bending curvature of 500 m^{-1} . **b** Comparison of sheet resistance variation between electrode and commercial ITO/PET with increasing bending curvatures. **c** Sheet resistance variation of a sample during 50,000 bending cycles, and the inserted image records the corresponding resistance of a sample under bending. **d** Sheet resistance variation as a function of stretching strain for electrodes, and the inserted SEM images depict two states of electrical pathways under stretching. Scale bar: $100 \mu\text{m}$. **e** Sheet resistance variation of a sample after set in ambient air for 200 days and corresponding values of the sheet resistance fluctuation.



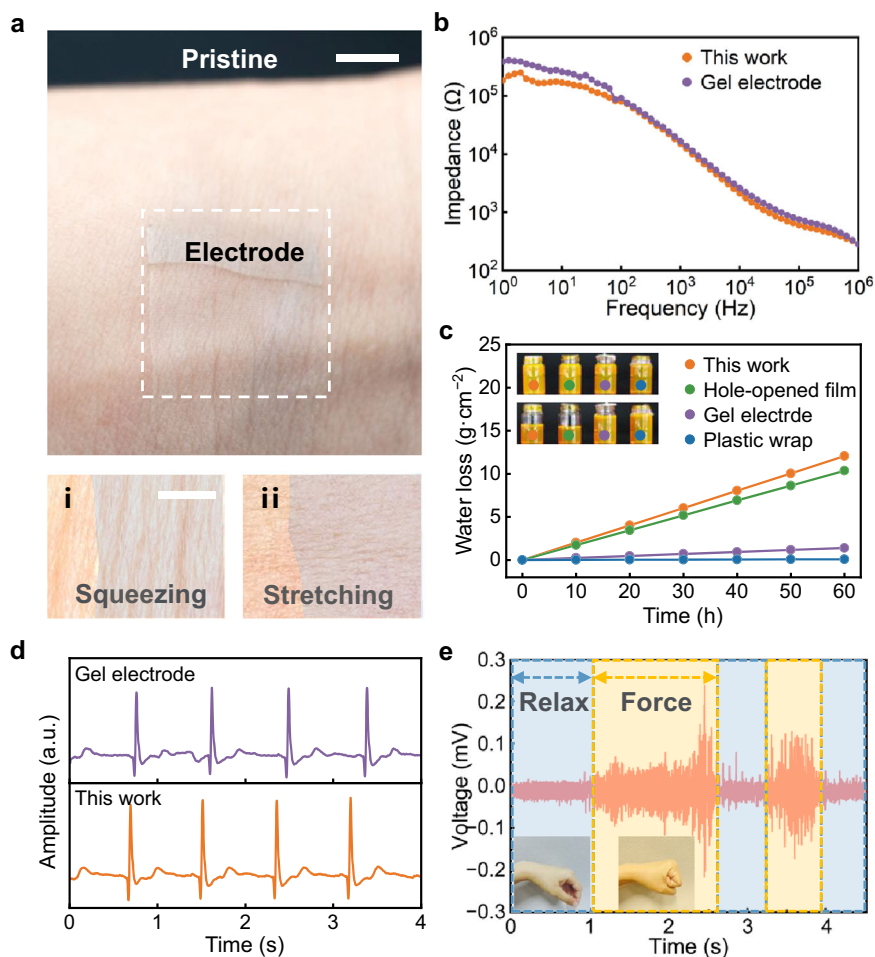
withstand the amount of stretching that occurs in the arm area in daily human life. For bioelectric signal monitoring, the contact impedance of the electrode with the skin was measured and compared with commercial gel electrodes (Fig. 5b). This result shows that this electrode has a similar contact resistance to gel electrodes above 100 Hz. This electrode has a lower contact impedance which decreases noise disturbance at the acquisition terminal than commercial gel electrode during the usual electrophysiological signal test range. Like commercial gel electrodes, preventing sweat from evaporating from the epidermis can cause signal distortion at the time of health monitoring. Thus, the air permeability of the electrode film was investigated by implementing an evaporation rate test experiment. Electrospun PVDF-TrFE film, GEL electrode, commercial plastic wrap, and electrode film covered of the bottles loaded with DI water. To observe the evaporation process, Rhodamine was added to the water for dyeing. The water content losses in the four bottles were compared after 60 hours under 60°C , 55% RH conditions. The water vapor loss permeated from the electrode film is a little bit higher than the electrospun PVDF-TrFE film due to the hole opening. GEL film and commercial plastic wrap have almost no water loss. By measuring the weight of four samples, it shows that the water weight in the four bottles linearly decreases over time, and the water loss rate of the electrode film is $0.2 \text{ g}\cdot\text{h}^{-1}$, which is close to the electrospun PVDF-TrFE sample ($0.17 \text{ g}\cdot\text{h}^{-1}$) and much higher than the GEL film ($0.02 \text{ g}\cdot\text{h}^{-1}$) and commercial plastic wrap film ($0.0001 \text{ g}\cdot\text{h}^{-1}$). This result demonstrates the good air permeability of the electrode film, which enables its great potential for on-skin applications. Figure 5d shows the ECG signal acquisition of the two different types of electrodes. It illustrates that the ultra-thin electrode exhibits obvious P-

Q-R-S-T characteristics peaks and that the signal strength is superior to those of commercial gel electrodes. The ultra-thin electrode records a higher magnitude of the signals with negligible noise fluctuation than the commercial gel electrode attributed to the high-fidelity conformality to the undulating skin and the good conductivity of the AgNW network, which provides higher surface charge density and surface electric displacement field for more precise extraction of electrical potential. This is mainly due to the smaller contact resistance between the electrode and the skin, and the voltage division of the signal at the contact impedance portion can be reduced, thus enhancing the signal voltage at the acquisition terminal. Furthermore, as shown in Supplementary Video 2, a sensor for real-time forearm muscles state monitoring was also fabricated by using this flexible transparent electrode. The contraction and relaxation of the forearm muscles were depicted in Fig. 5e. When the forearm exerts force, the hand grasps the fist, the voltage of the EMG signal increases immediately. These results indicate the potential of using this epidermal sensor to detect bioelectric signal.

Discussion

In summary, we propose an evaporation-induced approach to self-assemble AgNW into a regular-hole pattern. The formation of hole pattern is explored experimentally and theoretically. It is found that evaporation-induced liquid film rupture and subsequent fiber aggregation are vital for excellent optical, mechanical, and electrical properties. The electrode has an ultrathin thickness (about $5 \mu\text{m}$), high optical transmittance (87.8%), and low sheet resistance ($8.4 \Omega\cdot\text{sq}^{-1}$) with a low AgNW dosage ($9 \mu\text{g}\cdot\text{cm}^{-2}$). Moreover, it exhibits excellent durability during cyclic bending (50,000 times). Additionally, we demonstrated the potential applications of our electrode in

Fig. 5 | Adhesion and electrical performance of the electrode on skin for ECG and EMG signal monitoring. **a** Photograph of the ultra-thin electrode worn on the skin. Scale bar: 1 cm. **(i)** Photograph of the ultra-thin electrode worn on the squeezing skin. **(ii)** Photograph of the ultra-thin electrode worn on the stretching skin. **b** Impedance of the skin with electrode and gel electrode (reference) attached to the skin of the forearm. **c** Water loss rate of the four samples (ultra-thin electrode film, electrospun PVDF-TrFE film, GEL electrode) after 60 hours. **d** ECG recorded from this work and gel electrodes, respectively. **e** EMG signals recorded of different muscular states.



electronic skin sensor. More importantly, various can be realized by controlling the freezing dynamics to yield complex patterns of AgNW on various rigid and flexible substrates. With its versatility and designability, we believe that our evaporation-induced approach is beneficial for the fabrication of simple functional patterns, which are highly demanded in many advanced applications such as flexible electronic devices.

Methods

Fabrication of selective deposition of electrospun nanofiber film

Photolithography technique and wet etching were employed to obtain the silicon mold for the collector. The prepared silicon mold with the surface structure of square pyramid cavity arrays has been depicted in the former work²¹. The RCA-1 procedure was implemented for removing organic residue and films from a double oxidized (001) silicon wafer with about 1 μm oxide layer. A semi-automated mask aligner (MA6, SUSS) printed a 1.5 μm thick photoresist (RZJ-304) mask on the silicon wafer. The naked SiO_2 grids were etched in the etching solution (BOE), and the photoresist mask was removed by SYS9070 solution. The surface structure of square pyramid cavity arrays was obtained by etching the wafer in a hot potassium hydroxide solution (10 wt%, 70°C). A collector was prepared by depositing a silver film with a thickness of 300 nm on the silicon mold. PVDF-TrFE composites solution was prepared from PVDF-TrFE powder into a mixture of DMF and acetone with a mass ratio of 7:3 at the concentration of 15%, after stirring the solution for about 3 hours at 70°C. The solution was poured into a plastic syringe with a blunted 30 G needle. The electrospinning was done at 7 kV with a collecting distance of 10 cm and a feeding rate of 16.67 $\mu\text{L}\cdot\text{min}^{-1}$ for 1 min. The final freestanding PVDF-TrFE film can be obtained by stripping from the collector.

Fabrication of ultra-thin free-standing AgNW electrode

The electrospun nanofiber film was first dipped into a mixed solution of ethanol and DI water and dried naturally in the air. A commercial AgNW ink (nanowire length ranging from 50 to 150 μm , diameter ranging from 70 to 105 nm, 1 wt%, ethanol-water blend as dispersant, New Material Technology Company, Zhejiang, China) was dispersed uniformly in the mixed solution of ethanol and DI water to attain a concentration of 0.00015 wt%. The film was submerged in the silver nanowires dispersion and then dried in air, repeated several times to obtain the desired AgNW dosage.

Gas permeability test

Hole-opened PVDF-TrFE film, GEL electrode, commercial plastic wrap, and as-prepared electrode film covered of the bottles loaded with DI water. Each of the four bottles was filled with 2 mL of water and 7.5 mg of rhodamine dye. The four bottles were then put into a humidity-controlled chamber with a temperature of 60°C. The humidity was set at 55%. Concomitantly, the weight of bottles was recorded using an analytical scale to evaluate the water vapor loss.

Bending test

A 25 μm polyimide (PI) film was chosen as the substrate for the bending test. The electrode was transferred onto the PI film, where two ends were connected to the two Ag electrodes (with a thickness of 300 nm). The PI film was then fixed on a linear motion actuator and connected to the Keithley 2400 source meter to record the resistance change. The resistance was measured at the bending curvature of 500 m^{-1} at ambient conditions with the humidity of 55%. The period of the motion was set as 12 s, and the bending cycle was 50,000 times.

Bioelectric signal acquisition

The alternating current impedance of the electrodes and commercial gel electrodes was measured with an electrochemical workstation (Autolab). Two electrodes were used as working electrodes with an Ag/AgCl electrode as the reference electrode. ECG was measured from the front of the forearm using an ECG detector (BMD101), and EMG signals were acquired from the side of the forearm using a commercial EMG signal acquisition and processing device. All samples of electrodes were 2.5 cm × 2.5 cm square in shape, and the distance between the two samples was 7 cm.

Characterization

The morphologies of the electrodes were measured by the scanning electron microscope (S4700, Hitachi) and optical microscope. Optical images were obtained using the Nikon Lv150 microscope. Cross-section and morphology were captured with the FEI Nova Nano SEM 450. The transmittance spectrum was measured with the UV-vis-NIR spectrometer. The rupture of thin liquid film and hole-growth process simulations are performed using COMSOL Multiphysics software.

Data availability

The data used and analyzed during this study available from the corresponding author on reasonable request.

Code availability

All the custom codes deemed central to the conclusions are available from the corresponding authors upon reasonable request.

Received: 26 September 2023; Accepted: 24 April 2024;

Published online: 07 May 2024

References

- Zhang, Y., Ng, S.-W., Lu, X. & Zheng, Z. Solution-processed transparent electrodes for emerging thin-film solar cells. *Chem. Rev.* **120**, 2049–2122 (2020).
- Liu, Y., Li, C., Ren, Z., Yan, S. & Bryce, M. R. All-organic thermally activated delayed fluorescence materials for organic light-emitting diodes. *Nat. Rev. Mater.* **3**, 1–20 (2018).
- Kim, S. W. & Lee, S. Y. Transparent supercapacitors: from optical theories to optoelectronics applications. *Energy Environ. Mater.* **3**, 265–285 (2020).
- Hu, X. et al. A mechanically robust conducting polymer network electrode for efficient flexible perovskite solar cells. *Joule* **3**, 2205–2218 (2019).
- Fukuda, K., Yu, K. & Someya, T. The future of flexible organic solar cells. *Adv. Energy Mater.* **10**, 2000765 (2020).
- Zhao, H. et al. Ultrastretchable and washable conductive microtextiles by coassembly of silver nanowires and elastomeric microfibers for epidermal human-machine interfaces. *ACS Mater. Lett.* **3**, 912–920 (2021).
- Ma, X. et al. Highly permeable and ultrastretchable liquid metal micromesh for skin-attachable electronics. *ACS Mater. Lett.* **4**, 634–641 (2022).
- Reis Carneiro, M., Majidi, C. & Tavakoli, M. Multi-electrode printed bioelectronic patches for long-term electrophysiological monitoring. *Adv. Funct. Mater.* **32**, 2205956 (2022).
- Li, H. et al. Breathable and skin-conformal electronics with hybrid integration of microfabricated multifunctional sensors and kirigami-structured nanofibrous substrates. *Adv. Funct. Mater.* **32**, 2202792 (2022).
- Wang, B. & Facchetti, A. mechanically flexible conductors for stretchable and wearable e-skin and e-textile devices. *Adv. Mater.* **31**, 1901408 (2019).
- Heng, W., Solomon, S. & Gao, W. Flexible electronics and devices as human-machine interfaces for medical robotics. *Adv. Mater.* **34**, 2107902 (2022).
- Wu, H. et al. Materials, devices, and systems of on-skin electrodes for electrophysiological monitoring and human-machine interfaces. *Adv. Sci.* **8**, 2001938 (2021).
- Lu, L., Jiang, C., Hu, G., Liu, J. & Yang, B. Flexible noncontact sensing for human-machine interaction. *Adv. Mater.* **33**, 2100218 (2021).
- Kwon, Y.-T. et al. All-printed nanomembrane wireless bioelectronics using a biocompatible solderable graphene for multimodal human-machine interfaces. *Nat. Commun.* **11**, 3450 (2020).
- Herbert, R., Kim, J.-H., Kim, Y. S., Lee, H. M. & Yeo, W.-H. Soft material-enabled, flexible hybrid electronics for medicine, healthcare, and human-machine interfaces. *Materials* **11**, 187 (2018).
- Zhang, X.-R. et al. Patterned nanoparticle arrays fabricated using liquid film rupture self-assembly. *Langmuir* **39**, 10660–10669 (2023).
- Zhang, X.-R. et al. Transparent micropatterned conductive films based on highly-ordered nanowire network. *Nano Res.* **16**, 1–10 (2023).
- Fang, Y. et al. Solution-processed submicron free-standing, conformal, transparent, breathable epidermal electrodes. *ACS Appl. Mater. Interfaces* **12**, 23689–23696 (2020).
- Lin, Y. et al. High-resolution and large-size stretchable electrodes based on patterned silver nanowires composites. *Nano Res* **15**, 4590–4598 (2022).
- Zhang, N. et al. Flexible and transparent graphene/silver-nanowires composite film for high electromagnetic interference shielding effectiveness. *Sci. Bull.* **64**, 540–546 (2019).
- Xiong, J. et al. A deformable and highly robust ethyl cellulose transparent conductor with a scalable silver nanowires bundle micromesh. *Adv. Mater.* **30**, 1802803 (2018).
- Fan, Y. J. et al. Highly robust, transparent, and breathable epidermal electrode. *ACS Nano* **12**, 9326–9332 (2018).
- Tang, Q., Zou, M., Chang, L. & Guo, W. A super-flexible and transparent wood film/silver nanowire electrode for optical and capacitive dual-mode sensing wood-based electronic skin. *Chem. Eng. J.* **430**, 132152 (2022).
- Fang, Y. et al. High-performance hazy silver nanowire transparent electrodes through diameter tailoring for semitransparent photovoltaics. *Adv. Funct. Mater.* **28**, 1705409 (2018).
- Kang, S. et al. Capillary printing of highly aligned silver nanowire transparent electrodes for high-performance optoelectronic devices. *Nano Lett.* **15**, 7933–7942 (2015).
- Nayak, L., Mohanty, S., Nayak, S. K. & Ramadoss, A. A review on inkjet printing of nanoparticle inks for flexible electronics. *J. Mater. Chem. C.* **7**, 8771–8795 (2019).
- Layani, M., Berman, R. & Magdassi, S. Printing holes by a dewetting solution enables formation of a transparent conductive film. *ACS Appl. Mater. Interfaces* **6**, 18668–18672 (2014).
- Tokuno, T., Nogi, M., Jiu, J., Sugahara, T. & Sugauma, K. Transparent electrodes fabricated via the self-assembly of silver nanowires using a bubble template. *Langmuir* **28**, 9298–9302 (2012).
- Issakhani, S., Jadidi, O., Farhadi, J. & Bazargan, V. Geometrically-controlled evaporation-driven deposition of conductive carbon nanotube patterns on inclined surfaces. *Soft Matter* **19**, 1393–1406 (2023).
- An, B. W., Heo, S., Ji, S., Bien, F. & Park, J.-U. Transparent and flexible fingerprint sensor array with multiplexed detection of tactile pressure and skin temperature. *Nat. Commun.* **9**, 2458 (2018).
- Han, J., Yang, J., Gao, W. & Bai, H. Ice-templated, large-area silver nanowire pattern for flexible transparent electrode. *Adv. Funct. Mater.* **31**, 2010155 (2021).
- Xiong, J. et al. A tailorable spray-assembly strategy of silver nanowires-bundle mesh for transferable high-performance transparent conductor. *Adv. Funct. Mater.* **31**, 2006120 (2020).

33. Zhao, C. et al. Fluid driven self-assembly of woven Ag nanowire grid for ultra-flexible transparent electrodes. *Mater. Today Phys.* **20**, 100442 (2021).
34. Liu, S. L. et al. Fabrication and formation mechanism of electrospun spatially defined fibrous patterning structures on conductive and insulating substrates. *Key Eng. Mater.* **609**, 842–848 (2014).
35. Zhou, B. et al. Matrix-addressed crosstalk-free self-powered pressure sensor array based on electrospun isolated PVDF-TrFE cells. *Sens Actuators, A* **347**, 113993 (2022).
36. Shaw, T. Liquid redistribution during liquid-phase sintering. *J. Am. Ceram. Soc.* **69**, 27–34 (1986).
37. Ragelle, H. et al. Surface tension-assisted additive manufacturing. *Nat. Commun.* **9**, 1184 (2018).
38. Zhu, Z. et al. Shape and force analysis of capillary bridge between two slender structured surfaces. *Mech. Sci.* **6**, 211–220 (2015).
39. Chatzigiannakis, E., Jaensson, N. & Vermant, J. Thin liquid films: Where hydrodynamics, capillarity, surface stresses and intermolecular forces meet. *Curr. Opin. Colloid Interface Sci.* **53**, 101441 (2021).
40. De Gennes, P.-G. Wetting: statics and dynamics. *Rev. Mod. Phys.* **57**, 827 (1985).
41. Kheshgi, H. S. & Scriven, L. Dewetting: nucleation and growth of dry regions. *Chem. Eng. Sci.* **46**, 519–526 (1991).
42. Tammaro, D. et al. Elasticity in bubble rupture. *Langmuir* **34**, 5646–5654 (2018).
43. Yu, B. et al. Visualization of the interaction of water aerosol and nanofiber mesh. *Phys. Fluids* **33**, 092106 (2021).
44. Zhang, R. et al. In situ investigation on the nanoscale capture and evolution of aerosols on nanofibers. *Nano Lett.* **18**, 1130–1138 (2018).
45. Lam, T.-N. et al. Tunable mechanical and electrical properties of coaxial electrospun composite nanofibers of P(VDF-TrFE) and P(VDF-TrFE-CTFE). *Int. J. Mol. Sci.* **22**, 4639 (2021).
46. Adadi, N. et al. Electrospun fibrous PVDF-TrFe scaffolds for cardiac tissue engineering, differentiation, and maturation. *Adv. Mater. Technol.* **5** (2020).
47. Lee, B.-B., Ravindra, P. & Chan, E.-S. New drop weight analysis for surface tension determination of liquids. *Colloids Surf., A* **332**, 112–120 (2009).
48. Cai, Z. et al. Evaporation induced spontaneous micro-vortexes through engineering of the marangoni flow. *Angew. Chem. Int. Ed.* **59**, 23684–23689 (2020).
49. Noh, Y., Jeong, H., Park, J. & Lee, D. Charge-assisted coating of silver nanowire transparent conductive layer and application to flexible heater. *Surf. Interfaces* **32**, 102105 (2022).
50. Zhou, H. & Song, Y. Fabrication of silver mesh/grid and its applications in electronics. *ACS Appl. Mater. Interfaces* **13**, 3493–3511 (2021).
51. Sun, Q. Y. et al. Multilayer three-dimensional woven silver nanowire networks for absorption-dominated electromagnetic interference shielding. *Adv. Mater. Interfaces* **10**, 2202393 (2023).
52. Jiang, Z. et al. Highly stretchable metallic nanowire networks reinforced by the underlying randomly distributed elastic polymer nanofibers via interfacial adhesion improvement. *Adv. Mater.* **31**, 1903446 (2019).
53. Won, P. et al. Stretchable and transparent kirigami conductor of nanowire percolation network for electronic skin applications. *Nano Lett.* **19**, 6087–6096 (2019).
54. Ye, G. et al. A lamellibranchia-inspired epidermal electrode for electrophysiology. *Mater. Horiz.* **8**, 1047–1057 (2021).
55. Zhou, W. et al. Gas-permeable, ultrathin, stretchable epidermal electronics with porous electrodes. *ACS Nano* **14**, 5798–5805 (2020).

Acknowledgements

The authors would like to thank Prof. Xu Shaolin at Ultrafast Laser Micro-/Nanofabrication Laboratory, Southern University of Science and Technology, for the transmittance test.

Author contributions

C.Q. and Q.Y.S. conceived the idea and designed the experiment. C.Q. performed device fabrication with help from Y.C. and contributed to data collection. J.X.W. and Y.X.D. performed the simulations and possessed the signal. W.M. and H.Y.Y. obtained the funding. C.Q. wrote the whole paper. M.W. and S.F. reviewed the paper. All the authors gave valuable comments on this paper.

Competing interests

The authors declare no competing interests.

Additional information

Supplementary information The online version contains supplementary material available at <https://doi.org/10.1038/s41528-024-00314-2>.

Correspondence and requests for materials should be addressed to Min Wang.

Reprints and permissions information is available at <http://www.nature.com/reprints>

Publisher's note Springer Nature remains neutral with regard to jurisdictional claims in published maps and institutional affiliations.

Open Access This article is licensed under a Creative Commons Attribution 4.0 International License, which permits use, sharing, adaptation, distribution and reproduction in any medium or format, as long as you give appropriate credit to the original author(s) and the source, provide a link to the Creative Commons licence, and indicate if changes were made. The images or other third party material in this article are included in the article's Creative Commons licence, unless indicated otherwise in a credit line to the material. If material is not included in the article's Creative Commons licence and your intended use is not permitted by statutory regulation or exceeds the permitted use, you will need to obtain permission directly from the copyright holder. To view a copy of this licence, visit <http://creativecommons.org/licenses/by/4.0/>.

© The Author(s) 2024